Applied Surface Science 718 (2026) 164848

Contents lists available at ScienceDirect

Applied Surface Science

journal homepage: www.elsevier.com/locate/apsusc

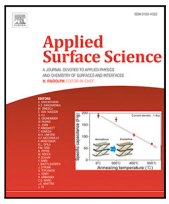

Full length article

On the surface energy of the Cantor alloy and its relation with surface composition

Lucrezia Berghenti, Margherita Marsili *, Maria Clelia Righi *

Department of Physics and Astronomy, University of Bologna, Viale Carlo Berti Pichat 6/2, Bologna, 40127, Italy

ARTICLE INFO

Keywords:
High entropy alloy
HEA
DFT
Surface
Surface energy

ABSTRACT

The relatively novel family of materials known as high entropy alloys, popular for exceptional mechanical properties, is currently gaining increasing attention also for remarkable surface properties. Nevertheless, due to the intrinsic difficulties that these materials pose to first-principle modelling, there is a lack of knowledge and understanding of the basics principles that govern their surface energetics. In this work the surface energy of the Cantor alloy was systematically investigated by means of density functional theory within a supercell approach that allows to tackle the effects of local atomic distributions. When properly accounting for the effective simulation slab stoichiometry the Cantor alloy surface energy displays an average value of 1.77 J/m^2, ranging between 1.65 J/m^2 and 1.95 J/m^2. Such values for the Cantor alloy's surface energy are well below those of its constituents also taking into account their variability, supporting the use of this material as anti-corrosion coating. Finally, by well assessing a slab total energy decomposition, required to account for the overall slab stoichiometry, an expression is derived which allows to infer the HEA surface energy, for any bulk configuration and surface termination, avoiding slab calculations.

1. Introduction

The single fcc-phase equiatomic CrMnFeCoNi alloy, known also as the Cantor alloy has distinguished itself for its excellent combination of strength, ductility and fracture resistance even at cryogenic temperature [1,2]. As a consequence, most of the available studies focus on its bulk properties. Nevertheless this alloy also possesses superior surface and tribological properties: such as anti-friction, antidiffusion, radiation and corrosion resistance qualities, making it extremely attractive also as a coating material [3]. In view of these applications, surface energy, defined as the energy cost per unit area upon creating a surface from an infinite bulk, is a key quantity. Indeed, the lower the surface energy, the more corrosion resistant the surface [4], low surface energies are linked to lower adhesions and friction coefficients, and surface energies have also a direct impact on alloy's intrinsic ductility.[5]

Despite their relevance and the vast amount of research on HEAs, there are only a handful of studies that provide first principle estimates of HEA's surface energy and a systematic analysis of their surface properties in general are extremely rare. In particular, besides the work of Zang et al. devoted specifically to the study of the surface energy of IrRuRhPdPt, NbMoTaTi and NbMoTaTiV alloys [6], and those of E. Mak et al. [5] and of Hun et al. [7] where first principle calculations of HEA surface energies were explicitly carried out for the purpose of quantifying the intrinsic ductility of body-centred-cubic multicomponents alloys, most of the studies that concern first-principle simulations of HEA's surfaces focus on other features such as surface segregation [8], and various molecule adsorption energies [9,10]. None of these studies concern specifically the case of the Cantor alloy and, moreover, the computational approach that is more often adopted, does not allow to address the effects of local chemical environments on the surface properties [11]. Indeed a systematic characterization of the Cantor alloy surfaces is currently missing together with a proper understanding of how specific local environments affect the surface energy.

In this work we employed density functional theory (DFT) to characterize the surface energy of the Cantor alloy. Our methodology, in which we average over an increasing number of randomly generated inequivalent supercells, allows to capture the intrinsic variability of this property and to understand it in terms of surface composition.

The paper is organized as follows: first the computational methodology is introduced (it is worth noting here that also basic procedures, such as the lattice constant determination, are far from being trivial due to both the disordered nature of the Cantor alloy and its complex magnetic behaviour); then the results on the surface energy of the pure constituent metals within a fcc geometry are presented; finally the Cantor alloy surface energy is analysed together with its intrinsic

* Corresponding author.
E-mail addresses: margherita.marsili@unibo.it (M. Marsili), clelia.righi@unibo.it (M.C. Righi).

https://doi.org/10.1016/j.apsusc.2025.164848
Received 23 May 2025; Received in revised form 3 October 2025; Accepted 6 October 2025
Available online 14 October 2025

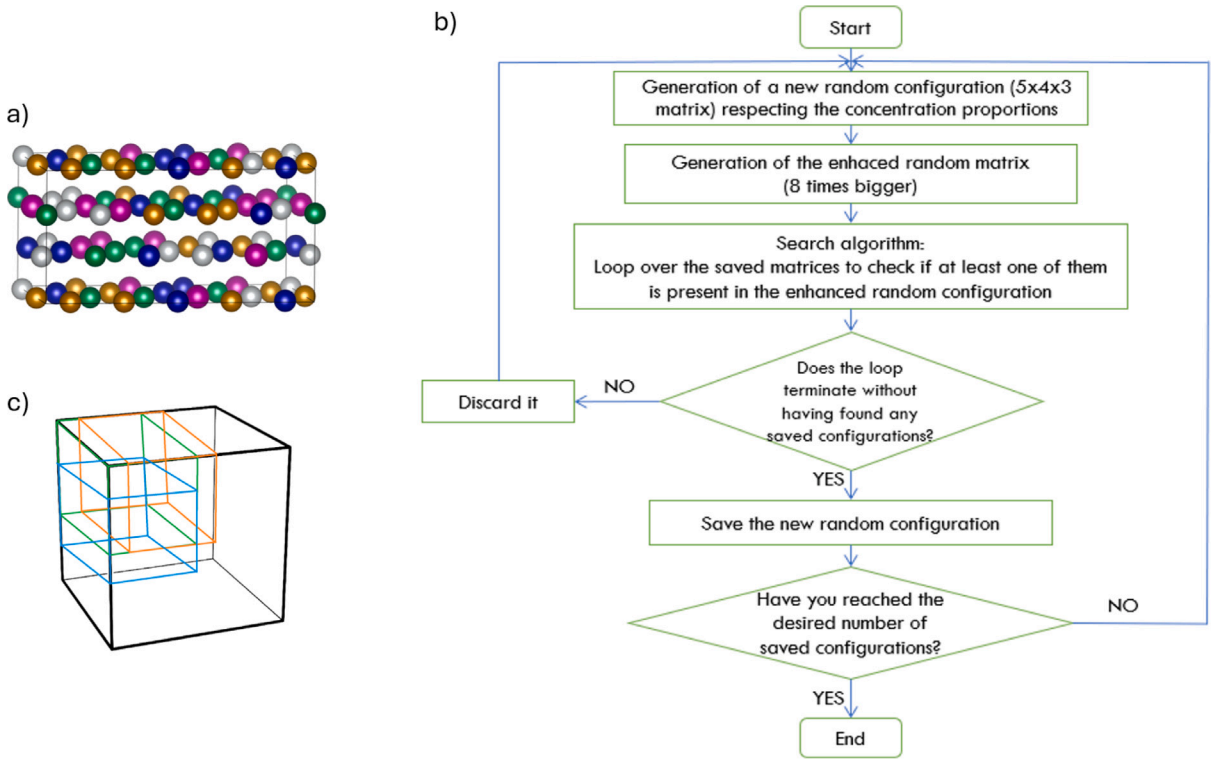

Fig. 1. (a) HEA fcc bulk unit cell of dimensions 5 × 4 × 3 modelled by considering the (111) surface as the xy-plane perpendicular to the z axis; (b) flowchart of the algorithm that generates inequivalent configurations. The image shows the step in which the generated random matrix is enhanced and the algorithm checks if inside it is contained at least one of the saved matrices, meaning that an equivalent matrix is already saved; (c) the black cube represents the enhanced matrix (of dimensions 10 × 8 × 6) whereas the coloured cubes some of its 5 × 4 × 3 portions.

variability which is mainly determined by the surface layer chemical composition.

2. Methods

2.1. Inequivalent bulk supercell generation

Several approaches have been used for DFT-based studies of HEAs. The most widely used one employs the so called special quasi-random structures (SQSs) [11–13]. SQS can be regarded as the best possible periodic unit cell representing a given random alloy. Such unit cells are built making sure that the correlation functions for the first few nearest neighbour atomic shells are as close as possible to those of the target random alloy. The clear advantage of the SQS approach is to obtain reliable estimates of the target properties by performing ab-initio calculations only on the *few* special structures. On the other hand, the SQS approach does not allow to gain insights on how local atomic distributions might affect the alloys properties.

To address the variability of the Cantor alloy surface energies due to local chemical configurations, instead, we generated random unit cells with fixed overall stoichiometry (constituents in equiatomic concentration) and we performed individual calculations on each of them. The physical quantities of interest were then computed for each random structure and averaged until their distribution was stable in terms of both average and standard deviation. In this way, it was made sure that the intrinsic variability of the observable was properly being captured. This kind of approach has also been used in several other studies, such as in [14] to study the suitability of HEAs for use within a nuclear reactor environment, in [15] to study the formation and structure of V–Zr amorphous alloy thin films and in [10] to reconstruct the adsorption energy distribution of oxygen intermediates on HEAs made of earth-abundant metals. The number of random configurations, required to converge the lattice parameter and cohesive energy is of the order of 1-2 tens, in agreement to what found in literature [10,14,16].

2.1.1. Non-equivalent configuration generation algorithm

The HEA fcc bulk was modelled considering the (111) surface as the xy-plane. Within this plane the lattice has a hexagonal geometry and perpendicularly to the plane the atoms geometrically arrange in an A-B-C stacking. We choose the bulk unit cell, shown in Fig. 1(a), it has dimensions (5,4,3) and therefore contains 60 atoms in total (20 atoms for each of the 3 inequivalent lattice planes). This cell size is large enough to avoid that artificial ordering, due to the imposed periodicity, affects significantly the energetics of the structure, indeed similar supercell sizes were also used in Refs. [7,14].

Due to translational invariance, different randomly generated unit cells could yield to the same infinite lattice. To generate non-equivalent random bulk supercells we proceeded as follows:

1. A new random 5 × 3 × 3 supercell is generated;
2. The generated random 5 × 4 × 3 supercell is “enhanced” to a 10 × 8 × 6 cell, by doubling it along all three dimensions. The 10 × 8 × 6 cell is shown in black in Fig. 1c;
3. Each previously generated (and stored) 5 × 4 × 3 supercell is compared to all possible 5 × 4 × 3 portions of the enhanced 10 × 8 × 6 cell. Examples of such portions are shown as coloured cubes in Fig. 1c;
4. If none of the previously generated 5 × 4 × 3 supercells is equivalent to any of these portions, the generated 5 × 4 × 3 supercell is stored with the others;
5. Else the 5 × 4 × 3 supercell is discarded and a new one is generated.

This procedure is repeated until the number of inequivalent configurations that guarantees the convergence of the lattice parameter and cohesive energy is reached.

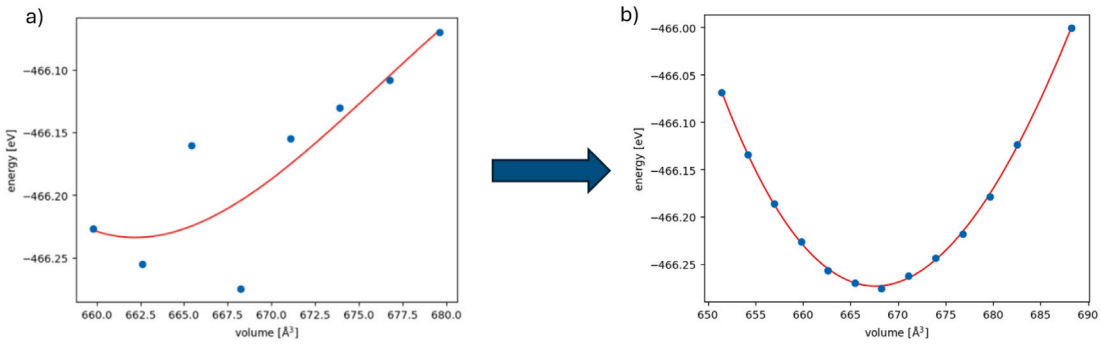

Fig. 2. (a) First set of relax calculations for different values of the lattice parameter a. The Murnaghan fit applied to HEA bulk unit cell produced scattered results; (b) Murnaghan fit produced by regularizing the previous plot following the protocol described in the text.

2.2. Bulk lattice constant determination

For each randomly generated supercell, at the optimal cutoff and k-mesh, the equilibrium lattice parameter is determined. Following a procedure which is completely standard within the solid state community, for each of the 15 different unit cell configurations, several relax calculations were performed varying the value of the lattice parameter. The optimal value of the lattice parameter for each configuration should have been, in principle, straightforwardly determined through a Birch-Murnaghan fit. However, when collecting the total energy against volume data, unpredictable scattered results, like the ones showed in Fig. 2(a), were obtained. This anomalous behaviour is a reflection of the complexity of the total energy landscapes of this material. Such complexity is due to the different magnetic properties of the Cantor alloy metal constituents: namely, Fe, Co, Ni are ferromagnetic elements, whereas Mn and Cr are antiferromagnetic. This diversity strongly influences the stability of the system. For example if Mn, antiferromagnetic, happens to be combined with ferromagnetic elements, Ni, Co and Fe, and another antiferromagnetic element, like Cr, the preferred antiparallel alignment of Mn spins cannot be completely satisfied [17]. Moreover, pure Mn in a fcc structure would be magnetically frustrated due to geometric constraints on nearest neighbour exchange interactions [18]. Additionally, in the particular case of HEAs, magnetic frustration also depends on local composition, i.e. the type and concentration of the different elements [17]. Therefore, to regularize the E_{tot} vs volume curves and to be able to identify the equilibrium lattice parameter for each configuration, a two step procedure was implemented: first of all a first set of relax calculations was carried out starting from a *good guess* of the input, unrelaxed, magnetic moments per atom, which assured smooth convergence at all lattice parameters, and secondly, a second round of relax calculations was run using as input the relaxed set of magnetic moments of the lowest energy structure obtained in the first run. For example, in the case shown in Fig. 2, the relaxed magnetic moments of the ~ 667.5 Å^3 volume cell of Fig. 2(a), were used as input magnetic moments for all the relax calculations whose results are collected in Fig. 2(b).

To summarize, for each randomly generated supercell the equilibrium lattice parameter was determined by:

1. performing a first set of relax calculations for different values of the lattice parameter a in order to identify the lattice parameter a_{min} giving minimum energy, as shown in Fig. 2 (a). In these step the initial magnetic moments μ_{MM} are set using Materials Project's [19] values of magnetic moments: $\mu_{\text{Co}} = 2$, $\mu_{\text{Cr}} = -2$, $\mu_{\text{Fe}} = 3$, $\mu_{\text{Mn}} = -2$, $\mu_{\text{Ni}} = 1$;
2. extracting the final relaxed magnetic moments μ_{output} belonging to the relaxed structure having minimum energy;
3. using these magnetic moments as input magnetic moments for new relax calculations at all lattice parameter and perform the Birch-Murnaghan fit, obtaining regularized curves as those shown in Fig. 2(b), and extracting the equilibrium lattice parameter a_{eq};

Once a_{eq} is determined, the structure is relaxed again and the cohesive energy $\epsilon_{\text{cohesive}}$ is obtained dividing the total free energy E_{bulk} by the number of atoms is the bulk.

Table 1
Methfessel-Fiorentini fit for different sets of number of layers: first using $N = 4, 7$, then $N = 4, 7, 10$ and eventually $N = 4, 7, 10, 13$ for a fixed configuration.

#Layers	ABC γ (J/m^2)	BCA γ (J/m^2)	CAB γ (J/m^2)
4	/	/	/
7	1.82	2.62	2.36
10	1.81	2.64	2.35
13	1.85	2.65	2.34

2.3. Slabs for surface energy calculations and surface energy convergence

The bulk unit cells used for this study are composed by the three inequivalent planes ABC, which differ not only by their geometrical stacking, but also for their chemical composition. Therefore, in order to characterize how local chemical configurations affect the surface energetics, we put care in using slabs where the same surface layer is exposed at both edges. For example considering the A-termination, some possible surface structures, with increasing numbers of layers, correspond to the stacking **ABCA**, **ABCABCA**, **ABCABCABCA**, etc. Following standard approaches, the number of layers making up the slab was identified through surface energy convergence. Namely the surface energies γ were determined using the Methfessel-Fiorentini method [20] where the total energy of the slab $E_{slab}(N)$ is considered as a function of the number N of layers, $E_{slab}(N) = 2\gamma \cdot A + N E_{bulk}$, A being the supercell area. The surface energy is then calculated from the angular coefficient obtained from the linear fit of this expression. An often underestimated advantage of using Methfessel-Fiorentini approach is that it does not oblige to refer to a value for the bulk cohesive energy, unlike when calculating the surface energy using directly the calculated value of the surface energy for increasing slab thicknesses. For all three termination of a bulk configuration we thus performed the fit for different sets of number of layers: first using $N = 4, 7$, then $N = 4, 7, 10$ and eventually $N = 4, 7, 10, 13$. The results are shown in Table 1. We see that the 4 to 7 layers fit is enough to obtain surface energy convergence. Finally because the details of the Cantor alloy energetics are strongly influenced by the initial magnetic moments that we set in input, it is worth mentioning that we used as initial magnetic moments for the slab the output magnetic moments of the three layers A, B and C, obtained from the bulk calculations.

a)

HEA, equilibrium from Murnaghan fit		
conf	a(eq) Å	Ecohesion (eV)
1	3.54	-7.77
2	3.55	-7.78
3	3.54	-7.78
4	3.55	-7.78
5	3.54	-7.77
6	3.54	-7.77
7	3.55	-7.77
8	3.54	-7.79
9	3.54	-7.78
10	3.54	-7.78
11	3.55	-7.77
12	3.54	-7.78
13	3.54	-7.78
14	3.53	-7.78
15	3.55	-7.79
mean	**3.54**	**-7.78**
std	0.01	0.01

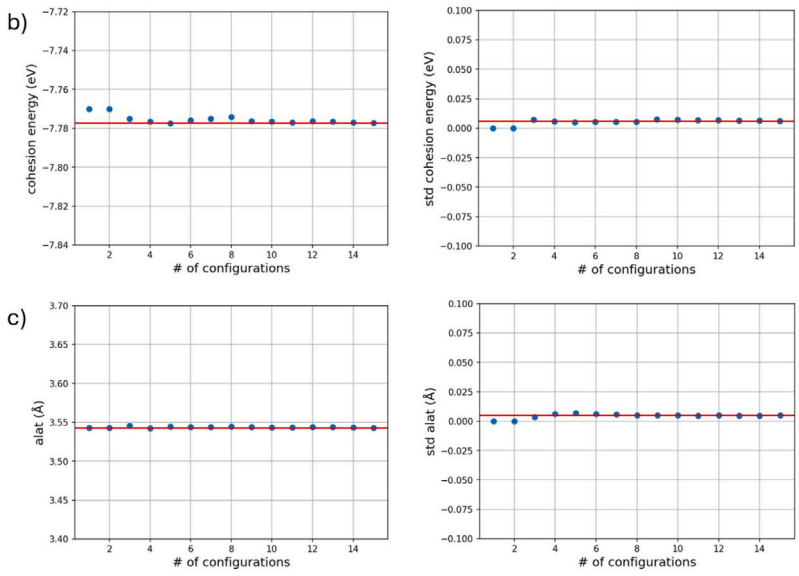

Fig. 3. (a) The table shows the values of the lattice parameter and cohesion energy obtained for each of the 15 inequivalent configurations. The mean values obtained for the lattice parameter and cohesion energy are respectively: $a_{eq} = (3.54 \pm 0.01)$ Å and $E_{coh} = (-7.78 \pm 0.01)$ eV. Running average for both the lattice parameter (b) and cohesion energy (c) of their mean and standard deviation: cohesion energy mean and its standard deviation as a function of the number of configurations used to calculate it.

2.4. Computational parameters

All computational simulations are performed using VASP (*Vienna Ab initio Simulation Package*) [21–23] which implements *Projector-Augmented-Wave* (PAW) pseudopotentials [24] and PBE-GGA exchange correlation functionals [25]. The bulk unit cell of our HEA is made of 3 layers parallel to the (111) plane and it has dimensions (x, y, z) = (5,4,3), for a total of 60 atoms, which is in line with the minimum size (54 atoms) required by the averaging method to converge the energy [7,14,26]. To obtain the optimal computational parameters, self-consistent field (scf) calculations were performed on a single random bulk configuration, at lattice parameter equal to a_{fcc}=3.6 Å, increasing the kinetic energy cutoff and k-point sampling until the energy per atom varied by less than 0.5 meV/atom. For all calculations the smearing was set to $\sigma = 0.1$ eV, and atomic positions were relaxed until the forces were converged within 0.05 eV/Å. Convergence was reached for a kinetic energy cutoff of 400 eV and a $(4 \times 5 \times 6)$ k-point grid . Both the convergence cutoff energy and k-points sampling compare well with the other available DFT studies [27,28]. For surface calculations we used 15 Å vacuum.

3. Results

3.1. Bulk properties

The 60-atom supercells used in this work have a randomly generated equiatomic distribution of atoms. In principle, at low temperatures, such structure would not be thermodynamically stable. Indeed, the stability of the HEAs random phase is guaranteed only by sufficiently high temperatures, when the contribution of the configurational entropy (maximized when all the components are present in the same proportion) to the Gibbs free energy becomes dominant [29]. Actually, coarse-grained Cantor alloy samples are found to be thermodynamically stable above 800 °C annealing temperature, kinetically stable below 450 °C annealing temperatures [29], with de-mixing and precipitations only being found after several years of intermediate annealing temperatures [30].

3.1.1. Lattice parameter

The procedure described in the Method (Section 2) has been applied for an increasing number of non-equivalent bulk configurations until the convergence of the cohesive energy and lattice parameter distributions was reached. Their tabulated values, together with the running average and running standard deviation, are shown in Fig. 3. It can be seen that 15 configurations are enough to converge the cohesive energy and the lattice parameter up to an error of 0.1%. The mean values obtained for the lattice parameter and cohesion energy are respectively: $a_{eq} = (3.54 \pm 0.01)$ Å and $\epsilon_{coh} = (-7.78 \pm 0.01)$ eV, both very close to the average values of lattice parameters and cohesion energy of the metal constituents fcc bulks, which correspond to 3.53 Å and −7.73 eV/atom respectively.

3.2. Surface properties of single transition metal constituents

Since the Cantor alloy has a fcc lattice structure, as a reference, we preliminarily study all the pure metal constituents in this crystalline structure, assessing the surface energies of their (111) faces within the same computational setup. The results are collected in Table 2.

The lower surface energies pertain to Ni and Co. Ni is most stable in the fcc crystalline structure, whereas Co most stable phase is the hcp one [32]. Actually, DFT calculations show that the fcc and hpc phases of Co are very close in energy, their relative stability strongly depending on the choice of the xc functional [33]. Higher surface energies are associated to Fe, Cr and Mn, whose most stable phase is also different from the fcc one (for brevity we will call this set of elements “high-surface energy species”) When compared with the surface energy of their most stable face in their equilibrium crystalline structure, shown in parenthesis in Table 2, we see that the surface energy of the high-surface energy elements further increases when they are set in their most stable crystalline phase. This is a consequence of the more stable bulk from which the formation of a surface is thus more energetically expensive. The electron configuration of the 3d transition metals elements that constitute the Cantor alloys display an increasingly filled d-shell that goes from half-filling, in the case of Cr and Mn, to an 8-electrons filling in the case of Ni. Despite possible complications due to magnetism, the computed surface energies follow the expected trend: when displayed against the d-shell occupation, the computed points belong to the decreasing interval of a parabola whose maximum is

Table 2
Surface energies of: (111)-surface of the HEA constituents fcc crystalline structures; the most stable structure, in parenthesis, from Legacy Materials Project Database [19,31] for the non-fcc elements Co(hpc), Fe (bcc), Mn (complex A12), Cr (bcc). The last row contains the surface energy descriptor values S_{surf} for the 5 atomic species Cr, Mn, Fe, Co, Ni of the Cantor alloy.

	Ni	Co	Fe	Mn	Cr	Mean	Std
Structure	fcc	fcc	fcc	fcc	fcc	/	/
Miller	(1 1 1)	(1 1 1)	(1 1 1)	(1 1 1)	(1 1 1)	/	/
γ (J/m^2)	1.94	2.08 (2.11)	2.32 (2.45)	2.64 (3.39)	2.75 (3.22)	2.01	0.10
S_{surf}	15.06	16.13	19.67	26.06	33.51	/	/

a)

Fiorentini-Methfessel surface energy γ (J/m²)															
conf	1	2	3	4	5	6	7	8	9	10	11	12	13	14	15
ABCABCA	1.70	2.41	1.82	2.56	2.15	2.11	2.20	2.69	2.66	1.88	1.58	1.92	2.02	1.92	2.40
BCABCAB	2.46	2.36	2.62	2.16	2.05	2.33	2.02	1.94	2.30	2.84	2.81	2.41	2.47	2.55	2.40
CABCABC	2.62	1.86	2.36	1.89	2.49	2.39	2.59	2.14	1.83	1.94	2.17	2.30	2.29	2.31	2.36

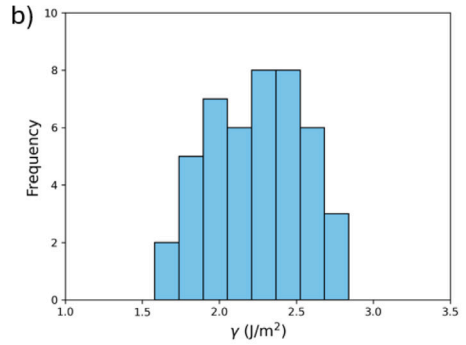

c)

HEA surface energy γ (J/m²)	
mean	std
2.25	0.30

constituents surface energy γ (J/m²) (111) - surface fcc lattice	
mean	std
2.35	0.35

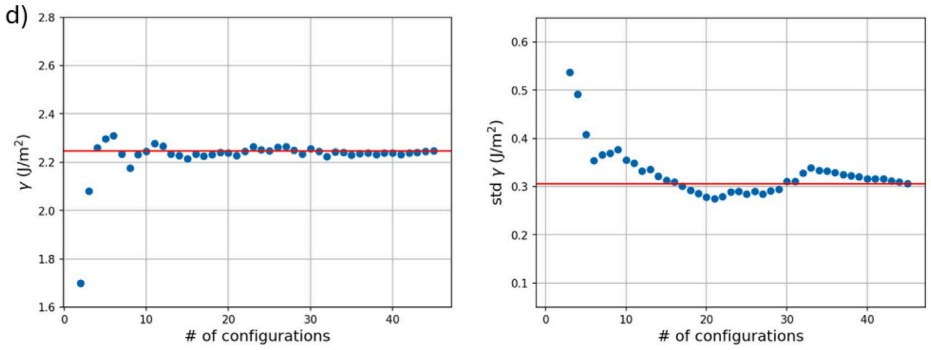

Fig. 4. (a) Table of the values of the surface energy of the 15 different bulk configurations having 3 different termination each; (b) histogram of the surface energy values; (c) mean and the standard deviation of the Cantor alloy and of its constituents surface energies; (d) running average of the surface energy and running standard deviation.

located at half-filling. In fact, it has been verified for both 3d [34] and 4d [35] transition metal series that the surface energy shows a parabolic trend which originates from the increasing d-band filling of the different metals. Indeed, within a simple bond-cutting model, the surface energy per atom is directly proportional to the d-bond energy. Therefore such parabolic dependence is a reflection of the parabolic dependence of the nearest-neighbour d-bonding strength against the number of d electron (maximal for half-full band), explained, within the Friedel model, in terms of filling of bonding (before half-filling) and anti-bonding (beyond half filling) d states [36].

3.3. Cantor alloy surface energy

Surface energies, computed using the Fiorentini-Methfessel method [20], described in the Methods Section 2, for the 45 surfaces are reported in 4, together with the corresponding running average and standard deviation. The stability of the distribution, in terms of both average and standard deviation, is reached using a number of bulk configurations equal to 15 (corresponding to 45 surface structures). The value of the surface energies for the 45 structures ranges between 1.58 J/m^2 and 2.84 J/m^2, averaging over the whole set we obtain $\gamma = (2.25 \pm 0.30)$ J/m^2. While the average surface energy of the Cantor alloy almost perfectly matches the average surface energy of the five constituents ($\overline{\gamma^{\text{const}}} = (2.35 \pm 0.35)$ J/m^2), its large variability (values range between 1.58 J/m^2 and 2.84 J/m^2) deserves further investigation. First of all we check how our calculations are affected by the fact that the two surfaces of each slab, despite having the same chemical composition, are not exactly equivalent due to a different sub-surface layer. Namely, from a chemical composition point of view, the slabs expose the same faces (either both A, B or C); however, the layer beneath the two surfaces is not of the same kind. For example considering the slab ABCABCA, the bottom surface has a B-type layer above it, while the top surface layer has a C-type layer below it.

To assess how much the coupling with the sub-surface layers affects the energetic of the surfaces, we apply systematic shifts in the xy-plane to the first and second superficial layers. The surface energy variations for these new configurations are shown in Fig. 5 (a). Shifting the surface layer with respect to the sub-surface one changes negligibly the surface energy, well below the variability of this quantity due to the specific

a)

conf - termination	γ no shift (J/m²)	Δγ 1-layer shift (J/m²)	Δγ 2-layers shift (J/m²)
2 - ABCABCA	2.50	-0.05	-0.05
2 - BCABCAB	2.59	-0.01	-0.03
2 - CABCABC	1.80	0.05	0.09
3 - ABCABCA	1.87	0.07	0.00
3 - BCABCAB	2.75	-0.02	-0.01
3 - CABCABC	2.39	0.04	0.06
4 - ABCABCA	2.73	0.00	-0.03
4 - BCABCAB	2.23	0.02	0.10
4 - CABCABC	1.91	0.04	0.01
5 - ABCABCA	2.13	-0.02	-0.03
5 - BCABCAB	1.95	-0.11	-0.05
5 - CABCABC	2.47	-0.02	-0.01

systematic shift	γ no shift	Δγ 1-layer shift	Δγ 2-layers shift
mean (J/m²)	2.28	0.00	0.00
std (J/m²)	0.34	0.05	0.05

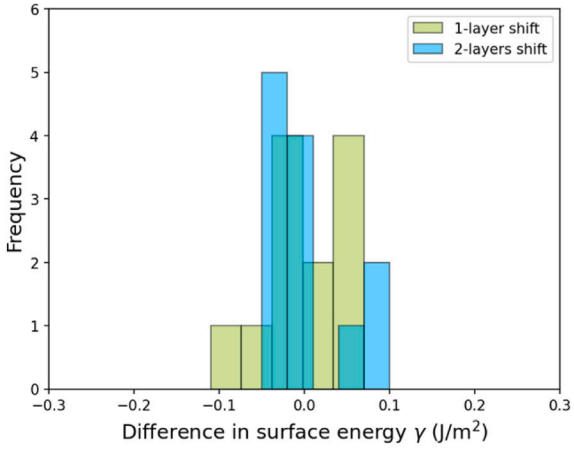

b)

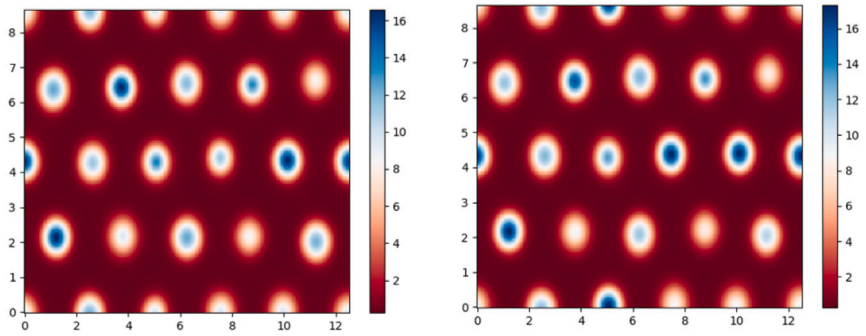

Fig. 5. (a) The first table illustrate HEA surface energies for the configurations 2, 3, 4, 5 (having 3 terminations each) obtained by the systematic shift of one and two layers below the superficial layer. The data are visualized in the histogram while the mean and standard deviation of these values are summarized in the table below. (b) The shows the charge density at the bottom and top surface planes of the slab ABCABCA. Even if the bottom surface has a B-type layer above while the top surface has a C-type layer below, the charge density at their respective surface planes presents the same pattern in both cases.

termination. This *decoupling* allows us to consider, to a good extent, the two faces as equivalent. Indeed, when looking at the charge density at the surface planes shown in Fig. 5 (b), very similar patterns can be recognized for the two faces.

The fact that the surface energy is almost completely independent on the relative position of the surface layers with respect to the bulk ones, suggests to look at the intrinsic properties of the surface layers themselves to account for the wide surface energy variability. In this view, it is worth noting that, while the bulk unit cell overall stoichiometry is preserved, the individual layers, therefore also the surface layers, are not equiatomic and their composition varies. It is then possible that the constituents concentration at the surface plays a major role. To this aim, we define an "expected" surface energy γ^{expec} in terms of constituents surface concentrations, as the weighted average of the constituents surface energies, the weights being the element concentration at the surface, namely:

$$\gamma^{\text{expec}} = \sum_{i=1}^{5} n_{\text{i}}\gamma_{\text{i}} \tag{1}$$

where the index i runs over the five constituents Ni, Co, Fe, Mn, Cr and the values for γ_{i} are those present in Table 2. The values of the computed surface energies γ against the corresponding expected surface energies γ^{expec} for each surface are shown in Fig. 6. The plot clearly shows an anti-correlation relation between the expected surface energy γ^{expec} and the surface energy γ which is actually calculated.

To understand this behaviour, we go back at Table 2 and observe that Ni and Co have lower surface energy than Fe, Mn and Cr. Therefore lower γ^{expec} values correspond to surfaces having a higher concentration of high surface energy elements; while higher γ^{expec} values correspond to surfaces having a higher concentration of low surface energy elements. In other words, ordering the different configurations in terms of γ^{expec}, is a way of actually ordering them in terms of the surface layer atomic species concentrations. This is indeed the case, as shown in Fig. 6(b), where surface energies γ are set against the sum of the concentrations of high surface energy elements (HSEE), namely $n^{surf}_{HSEE} = \frac{1}{N^{surf}_{at}} \sum_i N_i$ with i = Cr, Mn, Fe, and N^{surf}_{at} being the number of atoms of the surface of the slab.

3.4. A simple descriptor for the surface energy

Also in Ref. [6], for the cases of IrRuRhPdPt, NbMoTaTi and NbMoTaTiV HEAs, it was found that surface energies seemingly depended only on the species of atoms present in the HEA single surface layer. In the same paper, to account for the specific structure–property relationship, a surface energy descriptor was used in terms of the surface atoms period and group number, valence electron number (correlated with bandwidths, usually considered as an index of bond energy), and Pauling electronegativity, (governing charge transfer among different atoms and thus used to characterize adsorbate-surface bond distances [37]). Further physical insights on this descriptor can be found in Ref. [38] where it was first introduced to quantify surface energies material's dependence on a vast variety of materials.

We used a simplified version of the proposed descriptor, namely $S_{\text{surf}} = \sqrt[N]{\prod_{i=1}^{N} S_i}$, the geometric average, over the atoms belonging to the surface layer (labelled with the index i), of a chemical species-specific descriptor given by $S_i = \frac{S^i_d}{\chi_i}$ where S^i_d is the d-shell filling and χ_i is the Pauling electronegativity of the ith atom. As explained in Ref. [6], a geometric averaging procedure is used to define the surface descriptor instead of the arithmetic one. This choice is motivated by the need of capturing non-local environment effects, in an analogy with the single electron approximation in quantum mechanics, where complex non-local effects are better caught by geometric means [39].

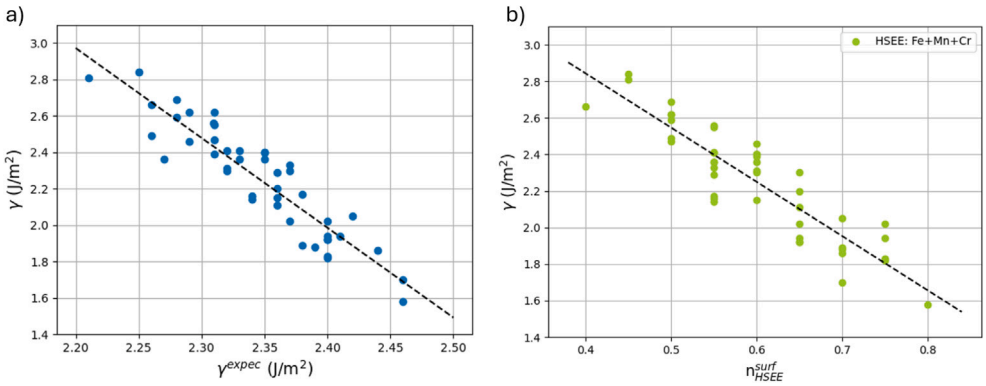

Fig. 6. (a) Surface energies calculated using the Methfessel-Fiorentini method compared to the surface energies estimated from the constituents concentrations at the surface. The plot shows an anticorrelation relation between the two quantities; correlation coefficient: −0.92, mean absolute error: 0.10 (J/m^2). (b) surface energy as a function of the concentration of high surface energy elements (Fe+Mn+Cr) at the surface; correlation coefficient: −0.90, mean absolute error: 0.11 (J/m^2).

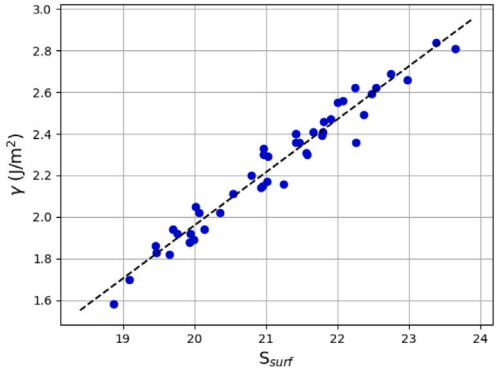

Fig. 7. Computed surface energy against the surface energy descriptor S_{surf}. The two quantities clearly correlate with a correlation coefficient of 0.98 and a mean absolute error of 0.054 J/m^2.

Surface energies are displayed against S_{surf} in Fig. 7 (a). The two quantities clearly correlate with a correlation coefficient of 0.98 and a mean absolute error of 0.05 J/m^2.

The S_i values for each of the 5 atomic species are reported in the last line of Table 2. Clearly the S_i index is able to discriminate between high surface energy elements (Cr, Mn, Fe), which have lower S_i, and low surface energy ones. At the same time, it also weights each element in a finer manner than n^{surf}_{HSEE} yielding a better correlation. However, while in this case γ displays a positive correlation with S_{surf}, in Ref. [6] the surface energies of the IrRuRhPdPt HEA show a quite different trend. First of all, surface energies and S_{surf} anticorrelate, secondly the correlation coefficient is ~ -0.7, quite lower, in absolute value, than what found here for the Cantor alloy's γ, and, finally, the IrRuRhPdPt HEA surface energy values range in much smaller intervals, namely $\sim$ 0.4–0.8 J/m^2, depending on the surface orientation. The extremely strong dependence of the computed γ on S_{surf} and especially its trend opposite both to γ^{expec} and to what found in the literature on S_{surf}, suggest that some important physical ingredient is missing.

3.5. Bond-cutting model analysis of the surface energy

As already mentioned when discussing the single constituents surface energies, within the Friedel model transition metals d-series bond energies ϵ_B have a parabolic dependence with d-band filling. The maximum of the parabola is located more or less at half-filling [35]. Therefore decreasing bond energies are expected following the series Cr, Mn, Fe, Co, Ni.

Bond energies ϵ_{bond} can be roughly estimated directly from bulk cohesive energies ϵ_{coh}, namely $\epsilon_{coh} = \frac{C^B}{2}\epsilon_B$, where C^B is the bulk coordination number. For FCC crystals $C^B_{FCC} = 12$, therefore $\epsilon^{FCC}_{bond} = \frac{1}{6}\epsilon_{coh}$. Indeed, the computed ϵ_{coh} (see S.I.) follow a decreasing trend along the series which then implies decreasing bond energies.

Within a simple bond-cutting model, the surface energy per atom is expected to be roughly proportional to the difference in bulk and surface atoms coordination numbers, i.e. the number of absent bonds per surface atom, times half the bond energy. The factor 1/2 originates from the fact that each bond is shared between two atoms. In the case of the (111) surface of FCC metals the number of absent bonds per atoms is equal to 3 so that energy loss per atom should approximately be $\sigma^{(111)}_{FCC} = 3 \cdot \frac{\epsilon^{FCC}_{bond}}{2} = \frac{1}{4}\epsilon_{coh}$. Therefore, when a surface displays a larger concentration of the atomic species with larger bond energies (for the Cantor alloys Cr, Mn, and Fe) larger surface energies would be expected, at odds with the anti-correlation found between γ and γ^{exp}, or similarly between γ and n^{surf}_{HSEE}.

The reason for such anti-correlation can be found with a more careful application of the bond-cutting model and keeping in mind that, when creating the ABCABCA-type slabs, the stoichiometry with respect to the equiatomic -ABC- bulk is actually being slightly changed. Indeed, building the ABCABCA slab could be imagined as appending to an equiatomic ABCABC one an additional layer A. In this view the total energy of the 7 layers slab E^{7L}_{SLAB} could be decomposed as:

$$E^{7L}_{SLAB} = E^{6L}_{BULK} - \sum_i \frac{N_i \cdot \epsilon^i_{coh}}{4} + \sum_i \frac{9}{12} N_i \cdot \epsilon^i_{coh} = E^{6L}_{BULK} + \sum_i \frac{1}{2} N_i \cdot \epsilon^i_{coh}, \tag{2}$$

where E^{6L}_{BULK} is the total energy of a 6 layers ABC bulk, N_i is the number of atoms of species i in the surface layer, ϵ^i_{coh} is the bulk cohesive energies of species i, the index i running along the Cr, Mn, Fe, Co, Ni series. Analysing the first expression of Eq. (2), this decomposition acquires a clear physical meaning: starting from a 6-layer bulk (-ABCABC-) of energy E^{6L}_{BULK}, a six layer slab ABCAB**C** is formed paying a price equal to $\sum_i \frac{N_i \cdot \epsilon^i_{coh}}{4}$ per atom to form a surface A plus a similar contribution to form a surface C. The latter contribution, i.e. the energy required to form the surface C, is immediately cancelled out when appending the second surface layer A to form the 7 layers slab ABCABC**A**. At the same time, upon appending the A layer, the energy of the bonds present within the A layer itself and between the A layer and the sub-surface C layer is gained, such energy amounts to $\sum_i 9 \cdot \frac{\epsilon^{FCC}_{bond}}{2} \cdot N_i = \sum_i \frac{9}{12} N_i \cdot \epsilon^i_{coh}$, being 9 the coordination number of the surface atoms of the (111) face of FCC metals.

While Eq. (2), has been derived for the (111) face of an FCC metal, similar reasoning could be applied for any other crystalline structure

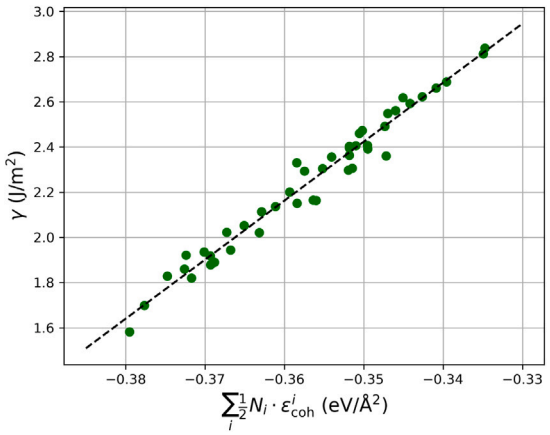

Fig. 8. Surface energy against $\sum_i \frac{1}{2} N_i \cdot \epsilon^i_{coh}$, a linear relationship is expected from Eq. (3). A correlation coefficient of 0.98 is found, with a mean absolute error of 0.041 J/m^2.

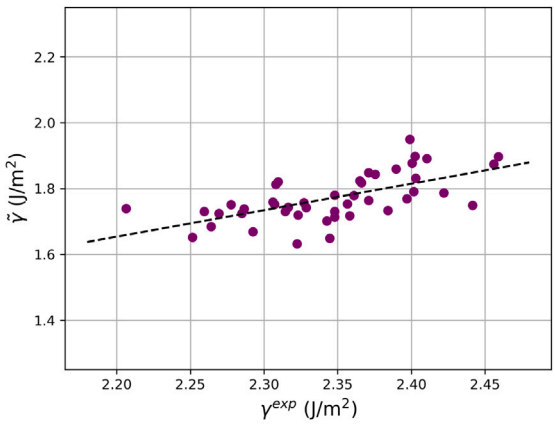

Fig. 9. Modified surface energy $\tilde{\gamma}$ vs surface energy expected from the species surface concentration. Correlation coefficient: 0.63; mean absolute error: 0.045 J/m^2.

and/or face. Indeed care should only be put into properly considering how the bulk cohesive energy is related to the bond energy, i.e. through the appropriate bulk coordination number, and in counting how many bonds are cut upon forming a surface, whose number can be easily determined for any FCC and BCC crystal face [40].

Inserting Eq. (2) in the expression surface energy γ its dependence on surface species concentration $\{N_i\}$ can made explicit obtaining:

$$\gamma = \frac{1}{2A}\left[E^{7L}_{SLAB} - N^{7L}\overline{\epsilon_{coh}}\right] = const + \frac{1}{2A}\sum_i \frac{1}{2} N_i \cdot \epsilon^i_{coh}. \tag{3}$$

Where N^{7L} is the total number of atoms of a 7-layers slab, and $\overline{\epsilon_{coh}}$ is the average cohesion energy of the equiatomic bulk -ABC- of the Cantor alloy, obtained by averaging over the 15 bulk configurations. Actually for each bulk configuration the specific ϵ_{coh} listed in Fig. 3a are used, but they are in fact extremely close to $\overline{\epsilon_{coh}}$. Fig. 8 shows γ as a function of $\sum_i \frac{1}{2} N_i \cdot \epsilon^i_{coh}$. A correlation coefficient of 0.98 is be found, with a mean absolute error of 0.041 J/m^2.

This result suggests that the computed γ are not properly a measure of surface reactivity but are instead related to how and by which amount the ABCABCA-type slab is off-stoichiometry. Indeed, they reflect how the presence (absence) of higher cohesive energy elements beyond stoichiometry is actually stabilizing (de-stabilizing) the slab with respect to the reference equiatomic condition, leading to smaller (larger) surface energies.

To obtain a quantity that relates directly to surface reactivity a $\overline{\epsilon_{coh}}$ pertaining to the ABCABCA-slab actual stoichiometry should be used. For this purpose it is possible to introduce $\tilde{\gamma}$ given by:

$$\tilde{\gamma} = \frac{1}{2A}\left[E^{7L}_{SLAB} - \sum_i N^{7L}_i \epsilon^i_{coh}\right], \tag{4}$$

where N^{7L}_i is the number of atoms of the species i in the 7-layers slab. Fig. 9 shows $\tilde{\gamma}$ against γ^{exp}. $\tilde{\gamma}$ average value is 1.77 J/m^2 with a small standard deviation of 0.07 J/m^2. Indeed, the vertical axis interval width has been specifically chosen to match those of Figs. 6, 7, 8, emphasizing how values, varying between 1.63 J/m^2 and 1.95 J/m^2, range in a much more limited interval with respect to γ. A slightly positive correlation coefficient of 0.63 is found between $\tilde{\gamma}$ and γ^{expec}, the surface energy expected from the surface concentration of the different species, with a mean absolute error of 0.045 J/m^2. As shown in Section S2 of the Supplementary Material, $\tilde{\gamma}$ anticorrelates with S_{surf} (correlation coefficient: −0.56, mean absolute error: 0.047 J/m^2), closer to the trend found for IrRuRhPdPt HEA in Ref. [6], where surface energies were estimated using as a reference the single constituent pure bulk cohesive energies multiplied by the constituent concentration, as done in our definition of $\tilde{\gamma}$. However, while in the case the IrRuRhPdPt HEA the computed surface energies are well above the average of the surface energies of its constituents (as extracted from the Materials Project DataBase [19]) in our case $\tilde{\gamma}$ are smaller, supporting the use of the Cantor alloy as anti-corrosion coating [41].

3.6. A simplified predictive expression for the surface energy

Despite the fact that γ does not provide a measure of surface reactivity, the almost perfect agreement by which Eq. (3) describes its behaviour (also displayed in Fig. 8) indicates that the decomposition of the slab energy in terms of a bulk contribution and a surface layer term is very reliable. Interestingly, both quantities stem only from bulk calculations. This means that the slab total energy could actually be inferred simply from bulk calculations and the knowledge of the surface composition. Moreover, this implies that the HEA surface energy, for any bulk configuration, could be predicted simply from the bulk calculation itself, by using the decomposition given by Eq. (3) in the definition of $\tilde{\gamma}$ (Eq. (4)), and obtaining:

$$\tilde{\gamma} = \frac{1}{2A}\left[E^{m}_{BULK} - \sum_i \left(N^{m+1}_i - \frac{1}{2}N_i\right)\cdot \epsilon^i_{coh}\right]. \tag{5}$$

where E^m_{BULK} is the total energy of the m-layers bulk, N^{m+1}_i is the number of atoms of species i in the $(m+1)$-layers slab, N_i is the number of atoms of species i in the surface layer, and ϵ^i_{coh} is the bulk cohesive energies of species i. In this work we took into account the equiatomic situation, nevertheless, Eq. (5) could be easily extended to study HEAs with non-equiatomic stoichiometry or with elemental substitutions. This would require tuning the bulk configuration generation algorithm to the target concentrations and computing the bulk cohesive energies of the novel chemical species.

Surface segregation effects were not considered in this work, the chemical composition of our surface layers being only randomly out of stoichiometry. While surface segregation is common in solid solutions, in the case of the Cantor alloy its role is being debated. Classical force field molecular dynamics and static calculations showed the tendency of Mn to segregate towards the surface [42], whereas ab-initio DFT calculations showed that surface segregation is negligible in vacuum and at room temperature, Mn and Cr segregating instead in the presence of oxygen [43]. Experimentally, it was shown that, up to 673 K annealing, the Cantor alloy surface composition is close to the nominal one. However, by raising further the temperature, the surface concentration of Mn and Ni rises [44].

The tendency of a chemical species towards surface segregation is often explained in terms of three competing driving forces: a surface

energy term, that favours the segregation of low surface energy elements; an alloy interaction term, related to the enthalpy of mixing and the number of bonds present within and among atomic planes; and, finally, an elastic strain energy term [42].

Within our approach, by systematically modifying the surface composition, surface segregation effects could be studied. The ab-initio DFT determination of the HEA alloy surface energy would naturally capture all three, surface energy, alloy interaction, and elastic strain energy, effects; whereas Eq. (5) would be limited to the surface energy contribution. Similarly to surface segragation, the proposed ab-initio approach could be also applied to study systematically the effect of bulk local short-range order on the surface energy. Indeed, the algorithm for the generation of non-equivalent bulk configurations should be modified to produce bulk supercells with target Warren-Cowley like parameter values [45]. In this way, the amount of "local short-range order" in the alloy would be controlled and its impact on surface energy could be revealed. The $\tilde{\gamma}$ model, on the other hand, would not be capable of considering clustering effects. In Section S3 of the Supplementary Materials, we show, with two illustrative examples, how to apply the proposed approach when varying stoichiometry or taking into account surface segregation.

4. Conclusions

In this work we systematically investigated how the randomly varying atomic distribution affects the surface energy of the Cantor alloy by means of DFT. For this purpose, we employed a supercell approach that allows to introduce the variability of the target quantities due to the specific atomic configurations. Random equiatomic 60-atoms bulk supercells were generated, carefully computing for each of them the equilibrium lattice constant and cohesive energy per atom. Due to the complex magnetic behaviour of this system a specific procedure was needed to regularize the total-energy vs lattice parameter curves. 15 non equivalent bulk configuration were enough to provide a stable distribution for the equilibrium lattice constant and the cohesive energy in terms of both average and standard deviation. Both quantities closely match the corresponding average values of the five metal constituents fcc bulks.

Converged surface energies were computed employing the standard Fiorentini-Methfessel procedure in which increasingly thick slabs exposing the same surface were built from equiatomic bulk configurations whose 60 atoms supercell consisted in 3 layers perpendicular to the (111) direction. Increasing the slab up to 7-layers was enough to reach converged value. In agreement with what found in Ref. [6] for the IrRuRhPdPt, NbMoTaTi, and NbMoTaTiV HEAs, the surface energetics seems dictated by the atomic configuration of the surface layer only, with very little dependence on the subsurface layers. However the dependence of the computed surface energies on the surface concentration of the different species displayed an opposite trend with respect to both what found in Ref. [6], and what would be expected by considering the relative amount of high surface energy or low surface energy species present at the surface.

To identify the source of this disagreement, by carefully applying the bond-cutting model, the slab total energy was decomposed in terms of a bulk and a surface layer contribution (Eq. (2)), from which a relation between the computed γ and surface concentration of atomic species was derived (Eq. (3)). This relation matches almost perfectly the computed quantities, assessing the validity of the slab total energy decomposition for this class of systems, and allowing to identify the source of disagreement of the computed γ with the expected trends. Indeed the computed γ appear not to be properly a measure of surface reactivity but are instead strongly influenced by how and by which amount the ABC(...)ABCA type slabs are off-stoichiometry.

When properly accounting for the simulation slab stoichiometry, the Cantor alloy surface energies shows a trend which is consistent with what present in the literature and a positive correlation with the γ^{expec}, meaning, for instance, that it is larger for those surfaces that have greater concentrations of high-surface energy metals. Its value range between 1.63 J/m^2 and 1.95 J/m^2, displaying an average value of 1.77 J/m^2, and standard deviation of 0.07 J/m^2. Therefore, also considering its intrinsic variability, the Cantor alloy's surface energy is significantly lower than that of its individual constituents, which implies improved anti-corrosion properties, as lower surface energy generally correlates with a more stable and less reactive surface. Finally, the favourable assessment of the slab total energy decomposition in terms of a bulk contribution and a surface layer term, permits the derivation of an expression that allows to infer the HEA surface energy, for any bulk configuration and surface termination, simply from the bulk calculations itself and the knowledge of the surface composition.

CRediT authorship contribution statement

Lucrezia Berghenti: Writing – original draft, Software, Investigation. **Margherita Marsili:** Writing – original draft, Supervision, Methodology, Formal analysis, Conceptualization. **Maria Clelia Righi:** Writing – review & editing, Supervision, Resources, Methodology, Funding acquisition, Conceptualization.

Declaration of competing interest

The authors declare the following financial interests/personal relationships which may be considered as potential competing interests: M. Clelia Righi reports financial support was provided by European Research Council. Margherita Marsili reports financial support was provided by European Union. If there are other authors, they declare that they have no known competing financial interests or personal relationships that could have appeared to influence the work reported in this paper.

Acknowledgements

These results are part of the "Advancing Solid Interface and Lubricants by First Principles Material Design (SLIDE)" project that has received funding from the European Research Council (ERC) under the European Union's Horizon 2020 research and innovation program (Grant agreement No. 865633).

All authors acknowledge the CINECA award under the ISCRA initiative, for the availability of high performance computing resources and the support by ICSC – Centro Nazionale di Ricerca in High Performance Computing, Big Data and Quantum Computing, funded by the European Union – NextGenerationEU.

Appendix A. Supplementary data

Supplementary material related to this article can be found online at https://doi.org/10.1016/j.apsusc.2025.164848.

Data availability

Data will be made available on request.

References

[1] Q. Ye, K. Feng, Z. Li, F. Lu, R. Li, J. Huang, Y. Wu, Microstructure and corrosion properties of CrMnFeCoNi high entropy alloy coating, Appl. Surf. Sci. 396 (2017) 1420–1426, http://dx.doi.org/10.1016/j.apsusc.2016.11.176, URL https://www.sciencedirect.com/science/article/pii/S0169433216326198.

[2] Z. Li, S. Zhao, R.O. Ritchie, M.A. Meyers, Mechanical properties of high-entropy alloys with emphasis on face-centered cubic alloys, Prog. Mater. Sci. 102 (2019) 296–345, http://dx.doi.org/10.1016/j.pmatsci.2018.12.003, URL https://www.sciencedirect.com/science/article/pii/S0079642518301178.

[3] J. Li, X. Meng, Y. Xie, A review on high entropy alloys coatings: Fabrication processes and property assessment, Adv. Eng. Mater. 21 (2019) 1900343, http://dx.doi.org/10.1002/adem.201900343.

[4] Z. Wang, D. Li, Y.-Y. Yao, Y.-L. Kuo, C.-H. Hsueh, Wettability, electron work function and corrosion behavior of CoCrFeMnNi high entropy alloy films, Surf. Coat. Technol. 400 (2020) 126222, http://dx.doi.org/10.1016/j.surfcoat.2020.126222.

[5] E. Mak, B. Yin, W. Curtin, A ductility criterion for bcc high entropy alloys, J. Mech. Phys. Solids 152 (2021) 104389, http://dx.doi.org/10.1016/j.jmps.2021.104389, URL https://www.sciencedirect.com/science/article/pii/S0022509621000776.

[6] Z. Yang, X. Li, W. Gao, Quantitative prediction of surface energy of high-entropy-alloys based on intrinsic descriptors, Surfaces Interfaces 42 (2023) 103442, http://dx.doi.org/10.1016/j.surfin.2023.103442, URL https://www.sciencedirect.com/science/article/pii/S246802302300812X.

[7] Y.-J. Hu, A. Sundar, S. Ogata, L. Qi, Screening of generalized stacking fault energies, surface energies and intrinsic ductile potency of refractory multicomponent alloys, Acta Mater. 210 (2021) 116800, http://dx.doi.org/10.1016/j.actamat.2021.116800.

[8] A. Ferrari, F. Körmann, Surface segregation in Cr-Mn-Fe-Co-Ni high entropy alloys, Appl. Surf. Sci. 533 (2020) 147471, http://dx.doi.org/10.1016/j.apsusc.2020.147471, URL https://www.sciencedirect.com/science/article/pii/S0169433220322285.

[9] J.K. Pedersen, T.A.A. Batchelor, A. Bagger, J. Rossmeisl, High-entropy alloys as catalysts for the CO_2 and CO reduction reactions, ACS Catal. 10 (3) (2020) 2169–2176, http://dx.doi.org/10.1021/acscatal.9b04343.

[10] G. Yuan, M. Wu, L. Ruiz Pestana, Density functional theory-machine learning characterization of the adsorption energy of oxygen intermediates on high-entropy alloys made of earth-abundant metals, J. Phys. Chem. C 127 (32) (2023) 15809–15818, http://dx.doi.org/10.1021/acs.jpcc.3c03404.

[11] A. Zunger, S.-H. Wei, L.G. Ferreira, J.E. Bernard, Special quasirandom structures, Phys. Rev. Lett. 65 (1990) 353–356, http://dx.doi.org/10.1103/PhysRevLett.65.353, URL https://link.aps.org/doi/10.1103/PhysRevLett.65.353.

[12] C. Niu, C. Jiang, D. Irving, Applications of Special Quasi-random Structures to High-Entropy Alloys, 2016, pp. 333–368, http://dx.doi.org/10.1007/978-3-319-27013-5_10.

[13] A. van de Walle, P. Tiwary, M. de Jong, D. Olmsted, M. Asta, A. Dick, D. Shin, Y. Wang, L.-Q. Chen, Z.-K. Liu, Efficient stochastic generation of special quasirandom structures, Calphad 42 (2013) 13–18, http://dx.doi.org/10.1016/j.calphad.2013.06.006, URL https://www.sciencedirect.com/science/article/pii/S0364591613000540.

[14] D.J.M. King, Investigation of High-Entropy Alloys for Use in Advanced Nuclear Applications (Master's thesis), University of Technology Sydney, Faculty of Science, 2016, URL http://hdl.handle.net/10453/52971, Open Access.

[15] D. King, S. Middleburgh, A. Liu, H. Tahini, G. Lumpkin, M. Cortie, Formation and structure of V–Zr amorphous alloy thin films, Acta Mater. 83 (2015) 269–275, http://dx.doi.org/10.1016/j.actamat.2014.10.016, URL https://www.sciencedirect.com/science/article/pii/S135964541400768X.

[16] C. Wagner, A. Ferrari, J. Schreuer, J.-P. Couzinié, Y. Ikeda, F. Körmann, G. Eggeler, E.P. George, G. Laplanche, Effects of Cr/Ni ratio on physical properties of Cr-Mn-Fe-Co-Ni high-entropy alloys, Acta Mater. 227 (2022) 117693, http://dx.doi.org/10.1016/j.actamat.2022.117693, URL https://www.sciencedirect.com/science/article/pii/S1359645422000805.

[17] C. Niu, C. Larosa, J. Miao, M. Mills, M. Ghazisaeidi, Magnetically-driven phase transformation strengthening in high entropy alloys, Nat. Commun. 9 (2018) http://dx.doi.org/10.1038/s41467-018-03846-0.

[18] J.M.D. Coey, Magnetism and Magnetic Materials, Cambridge University Press, 2009.

[19] A. Jain, S.P. Ong, G. Hautier, W. Chen, W.D. Richards, S. Dacek, S. Cholia, D. Gunter, D. Skinner, G. Ceder, K.a. Persson, The materials project: A materials genome approach to accelerating materials innovation, APL Mater. 1 (1) (2013) 011002, http://dx.doi.org/10.1063/1.4812323, URL http://link.aip.org/link/AMPADS/v1/i1/p011002/s1&Agg=doi.

[20] V. Fiorentini, M. Methfessel, Extracting convergent surface energies from slab calculations, J. Phys.: Condens. Matter. 8 (36) (1996) 6525, http://dx.doi.org/10.1088/0953-8984/8/36/005.

[21] G. Kresse, J. Hafner, Ab initio molecular dynamics for liquid metals, Phys. Rev. B 47 (1993) 558–561, http://dx.doi.org/10.1103/PhysRevB.47.558.

[22] G. Kresse, J. Furthmüller, Efficiency of ab-initio total energy calculations for metals and semiconductors using a plane-wave basis set, Comput. Mater. Sci. 6 (1) (1996) 15–50, http://dx.doi.org/10.1016/0927-0256(96)00008-0.

[23] G. Kresse, J. Furthmüller, Efficient iterative schemes for ab initio total-energy calculations using a plane-wave basis set, Phys. Rev. B 54 (1996) 11169–11186, http://dx.doi.org/10.1103/PhysRevB.54.11169.

[24] P.E. Blöchl, Projector augmented-wave method, Phys. Rev. B 50 (1994) 17953–17979, http://dx.doi.org/10.1103/PhysRevB.50.17953.

[25] J.P. Perdew, K. Burke, M. Ernzerhof, Generalized gradient approximation made simple, Phys. Rev. Lett. 77 (1996) 3865–3868, http://dx.doi.org/10.1103/PhysRevLett.77.3865.

[26] S. Zhao, G.M. Stocks, Y. Zhang, Stacking fault energies of face-centered cubic concentrated solid solution alloys, Acta Mater. 134 (2017) 334–345, http://dx.doi.org/10.1016/j.actamat.2017.05.001, URL https://www.sciencedirect.com/science/article/pii/S1359645417303671.

[27] J. Kumar, A. Linda, M. Sadhasivam, K. Pradeep, N.P. Gurao, K. Biswas, The effect of al addition on solid solution strengthening in CoCrFeMnNi: Experiment and modelling, Acta Mater. 238 (2022) 118208, http://dx.doi.org/10.1016/j.actamat.2022.118208, URL https://www.sciencedirect.com/science/article/pii/S1359645422005894.

[28] C. Wang, K. Han, X. Liu, Y. Zhu, S. Liang, L. Zhao, M. Huang, Z. Li, First-principles study of hydrogen-vacancy interactions in CoCrFeMnNi high-entropy alloy, J. Alloys Compd. 922 (2022) 166259, http://dx.doi.org/10.1016/j.jallcom.2022.166259, URL https://www.sciencedirect.com/science/article/pii/S0925838822026500.

[29] B. Cantor, Local nanostructure in multicomponent high-entropy materials, High Entropy Alloy. Mater. 2 (2) (2024) 277–306, http://dx.doi.org/10.1007/s44210-024-00040-4.

[30] F. Otto, A. Dlouhý, K. Pradeep, M. Kuběnová, D. Raabe, G. Eggeler, E. George, Decomposition of the single-phase high-entropy alloy CrMnFeCoNi after prolonged anneals at intermediate temperatures, Acta Mater. 112 (2016) 40–52, http://dx.doi.org/10.1016/j.actamat.2016.04.005, URL https://www.sciencedirect.com/science/article/pii/S1359645416302610.

[31] R. Tran, Z. Xu, B. Radhakrishnan, D. Winston, W. Sun, K.A. Persson, S.P. Ong, Surface energies of elemental crystals, Sci. Data 3 (1) (2016) 160080, http://dx.doi.org/10.1038/sdata.2016.80.

[32] C. Houska, B. Averbach, M. Cohen, The cobalt transformation, Acta Metall. 8 (2) (1960) 81–87, http://dx.doi.org/10.1016/0001-6160(60)90088-2, URL https://www.sciencedirect.com/science/article/pii/0001616060900882.

[33] R. Kingsbury, A.S. Gupta, C.J. Bartel, J.M. Munro, S. Dwaraknath, M. Horton, K.A. Persson, Performance comparison of r^2SCAN and SCAN metaGGA density functionals for solid materials via an automated, high-throughput computational workflow, Phys. Rev. Mater. 6 (2022) 013801, http://dx.doi.org/10.1103/PhysRevMaterials.6.013801, URL https://link.aps.org/doi/10.1103/PhysRevMaterials.6.013801.

[34] J.-Y. Lee, M. Punkkinen, S. Schönecker, Z. Nabi, K. Kádas, V. Zólyomi, Y. Koo, Q.-M. Hu, R. Ahuja, B. Johansson, J. Kollár, L. Vitos, S. Kwon, The surface energy and stress of metals, Surf. Sci. 674 (2018) 51–68, http://dx.doi.org/10.1016/j.susc.2018.03.008, URL https://www.sciencedirect.com/science/article/pii/S0039602818300852.

[35] M. Methfessel, D. Hennig, M. Scheffler, Trends of the surface relaxations, surface energies, and work functions of the 4d transition metals, Phys. Rev. B 46 (1992) 4816–4829, http://dx.doi.org/10.1103/PhysRevB.46.4816, URL https://link.aps.org/doi/10.1103/PhysRevB.46.4816.

[36] A. Sutton, A. Sutton, U. Sutton, Electronic structure of materials, in: Oxford science publications, Clarendon Press, 1993, URL https://books.google.it/books?id=cPXDQgAACAAJ.

[37] H. Xin, A. Holewinski, S. Linic, Predictive structure–reactivity models for rapid screening of Pt-based multimetallic electrocatalysts for the oxygen reduction reaction, ACS Catal. 2 (1) (2012) 12–16, http://dx.doi.org/10.1021/cs200462f.

[38] B. Li, X. Li, W. Gao, Q. Jiang, An effective scheme to determine surface energy and its relation with adsorption energy, Acta Mater. 212 (2021) 116895, http://dx.doi.org/10.1016/j.actamat.2021.116895, URL https://www.sciencedirect.com/science/article/pii/S1359645421002755.

[39] D. Vollhardt, Dynamical mean-field theory of electronic correlations in models and materials, AIP Conf. Proc. 1297 (1) (2010) 339–403, http://dx.doi.org/10.1063/1.3518901, arXiv:https://pubs.aip.org/aip/acp/article-pdf/1297/1/339/11407723/339_1_online.pdf.

[40] J. Mackenzie, A. Moore, J. Nicholas, Bonds broken at atomically flat crystal surfaces—I: Face-centred and body-centred cubic crystals, J. Phys. Chem. Solids 23 (3) (1962) 185–196, http://dx.doi.org/10.1016/0022-3697(62)90001-X, URL https://www.sciencedirect.com/science/article/pii/002236976290001X.

[41] Y. Hou, B. Dou, C. Xie, F. Sun, S. Rioual, B. Lescop, K. Ogle, A. Miche, O. Gharbi, M. Turmine, V. Vivier, On the corrosion resistance of the CoCrFeMnNi high entropy alloys in chloride-containing sulfuric acid solutions, Appl. Surf. Sci. 681 (2025) 161487, http://dx.doi.org/10.1016/j.apsusc.2024.161487, URL https://www.sciencedirect.com/science/article/pii/S0169433224022025.

[42] P. Wynblatt, D. Chatain, Modeling grain boundary and surface segregation in multicomponent high-entropy alloys, Phys. Rev. Mater. 3 (2019) 054004, http://dx.doi.org/10.1103/PhysRevMaterials.3.054004, URL https://link.aps.org/doi/10.1103/PhysRevMaterials.3.054004.

[43] A. Ferrari, F. Körmann, Surface segregation in Cr-Mn-Fe-Co-Ni high entropy alloys, Appl. Surf. Sci. 533 (2020) 147471, http://dx.doi.org/10.1016/j.apsusc.2020.147471, URL https://www.sciencedirect.com/science/article/pii/S0169433220322285.

[44] J. Ledieu, M. Feuerbacher, C. Thomas, M.-C. de Weerd, S. Šturm, M. Podlogar, J. Ghanbaja, S. Migot, M. Sicot, V. Fournée, The (110) and (320) surfaces of a Cantor alloy, Acta Mater. 209 (2021) 116790, http://dx.doi.org/10.1016/j.actamat.2021.116790, URL https://www.sciencedirect.com/science/article/pii/S1359645421001701.

[45] S.M. Aspera, R.L. Arevalo, H. Nakanishi, H. Kasai, First principles study of surface stability and segregation of PdRuRh ternary metal alloy system, Surf. Sci. 671 (2018) 51–59, http://dx.doi.org/10.1016/j.susc.2018.02.005, URL https://www.sciencedirect.com/science/article/pii/S003960281730599X.